The Role of Water on Postcombustion CO_2 Capture by Vacuum Swing Adsorption: Bed Layering and Purge to Feed Ratio

Gang Li, Penny Xiao, Jun Zhang, and Paul A. Webley
Cooperative Research Centre for Greenhouse Gas Technologies (CO2CRC), Dept. of Chemical and Biomolecular Engineering, The University of Melbourne, Parkville, VIC 3010, Australia

Dong Xu
Energy Innovation Technology Research Center, 2 Street, Future Science & Technology Park North, Changping District, Beijing, 102209, China

DOI 10.1002/aic.14281

The influence of water vapor on the adsorption of CO_2 in carbon capture by vacuum swing adsorption (VSA) was described. VSA experiments with single and multilayered columns using alumina and zeolite 13X were conducted to understand the migration of water. The penetration depth of water in the column could be controlled by maintaining the purge-to-feed ratio above a critical value. At high water content in the feed (>4%), employment of a water adsorbing prelayer was essential to prevent failure of the carbon capture process. A simple axial working capacity model predicts the penetration depth of water in the column for a given feed temperature and adsorption isotherm, and the layering ratio can be selected accordingly. Although water is detrimental to CO_2 capture with polar adsorbents, long-term recovery of CO_2 is still possible by appropriate layering and ensuring an adequate purge-to-feed ratio. © 2013 American Institute of Chemical Engineers *AIChE J*, 60: 673–689, 2014

Keywords: vacuum swing adsorption, carbon capture, water, purge-to-feed ratio, multilayered column

Introduction

Vacuum swing adsorption (VSA) is a promising technology for capturing CO_2 from a variety of industrial flue gases. Previous experimental and simulation studies have shown that adsorption-based capture of CO_2 from dry flue gases can be achieved with high purity (>90%) and recovery (>80%).[1–5] However, for real flue gas, the presence of heavy impurities, depending on the fuel sources, such as H_2O, SO_x, NO_x and so forth, may severely affect the CO_2 capture process.[6,7] Particularly, flue gas is invariably saturated with water (3–10%) and is, therefore, the major "impurity," significantly lowering the adsorption capacity of CO_2 on polar adsorbents, such as most of the zeolites[8] and metal organic frameworks.[9] Some aminosilica materials[10,11] such as amine tethered or polyethyleneimine impregnated mesoporous silica show considerable CO_2 uptake in the presence of water vapor; however, owing to the chemisorption nature, the long-term chemical stability and regenerability of the aminosilica materials[12] not yet comparable to the benchmark 13X zeolites under VSA conditions. Nevertheless, CO_2 adsorption capacity on 13X zeolite is extremely vulnerable to water vapor.[13] Because of its large dipole moment, water bonds strongly with the cations in zelites, characterized by a high heat of adsorption (e.g., >50 kJ/mol on zeolite 13X). There have been many published works on the removal of both water vapor and CO_2 by adsorption processes, but they are confined to the field of air prepurification, where the concentration of CO_2 is limited to ppm levels.[14,15] One exception is the recent simulation work by Ribeiro et al.[16] regarding the effect of water vapor on purification of the light component H_2. However, process study on the recovery of heavy components (CO_2 in this case) from humid gases is still rare in literature. Our preliminary work suggested that simultaneous carbon capture and water removal can be integrated with a single VSA unit, which is believed more cost competitive than that using predrying stage.[6] However, in that work, only a single adsorbent layer (13X) was used to treat flue gases with low water content. Most importantly, the key factors controlling the CO_2/H_2O concentration profiles and their interactions in the column remain unresolved. It is challenging to capture CO_2 from gases with even higher water content (>4% v/v) which may prevail at real flue gas temperatures.

Conversely, as few adsorbents work equally well for all gas components, adding a prelayer for water removal seems necessary for protecting the CO_2 adsorption layer. Using a layered bed configuration is not a new concept in adsorption-based technologies.[15,17–28] The advantage of using a multilayered column over multicolumns in series is clear in that it reduces the capital cost. Furthermore, the proportion of the layers can be adjusted according to the feed composition. Layered columns have been used in pressure swing adsorption (PSA) processes for several applications, such as:

Additional Supporting Information may be found in the online version of this article.

Correspondence concerning this article should be addressed to P. Webley at paul.webley@unimelb.edu.au.

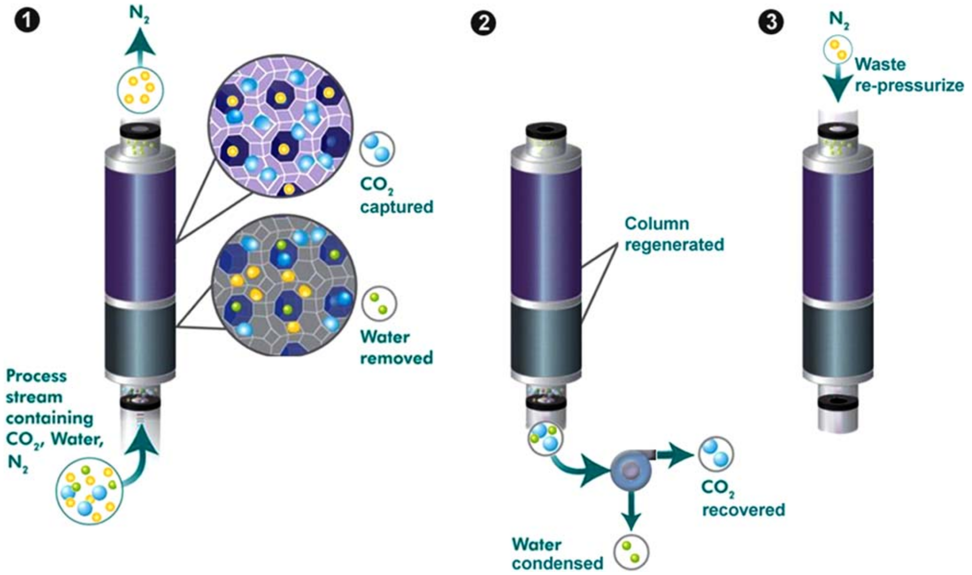

Figure 1. Three step cycle design for CO_2/H_2O VSA with double/multilayered layered column: step 1, adsorption; step 2, countercurrent evacuation; step 3, repressurization.

[Color figure can be viewed in the online issue, which is available at wileyonlinelibrary.com.]

(1) air prepurification,[14,15,21] with an activated alumina layer to remove mainly H_2O followed by a zeolite layer to remove CO_2 (ppm level) and the other components, in which an extra catalyst layer can be added in between to convert the trace hydrocarbons and carbon monoxide into CO_2 and water and get removed by the subsequent zeolite layers;[29] (2) H_2 purification;[23–25,28] (3) upgrading methane from $CH_4/CO_2/N_2$ mixtures.[18,19] Moreover, layered columns were also used in temperature swing adsorption for air drying.[17,30] The general principle of using a layered bed involves using a weak adsorbent with a more linear isotherm (e.g., activated carbon) and hence larger working capacity to remove the bulk impurity at the inlet of the bed followed by a strong adsorbent with favorable isotherm to eliminate the residual traces.[15]

Also, optimization of the ratio of the column layers is important for maximizing the use of each adsorbent and minimizing the adsorber size. This optimal ratio is normally determined by comparing the performance of the system over a range of experiments/simulations at certain constraints under specific operation conditions,[15,17,23,25] for example, the requirement of a minimum product purity. Nikolić et al. developed a strategy, named state transition network representation, to optimize multilayered PSA processes.[31] Chlendi and Tondeur[20] studied the dynamics and optimization of layered columns in PSA with a pseudo-characteristics method and they discovered that the transfer of the concentration waves from one layer to the other showed phenomena of refraction, diffraction, dispersion, and interference similar to light rays in optics. Pigorini and LeVan[32] solved the periodic concentration profile and the penetration depth of the shock wave in layered isothermal PSA by using local equilibrium theory.

All the above work involves the purification of the light products (H_2, CH_4, or air) harvested from the top of the column, with little concern on the heavy components. In this work, we focus on the recovery rate and purity of the heavy CO_2 with simultaneous removal of H_2O from the bottom of the column. Therefore, a different process design is required. One typical issue is that the conventional light component purge step[16] normally used for column regeneration is inappropriate in this work as it will dilute the heavy product CO_2; instead, an “internal purge” can be highly desirable for sweeping off the heavier contaminant H_2O.

The aim of this study is to understand the controlling factors on the formation, migration, and stabilization of the water concentration front and to develop a convenient model to determine the penetration depth of water in a typical CO_2 VSA column. This study was carried out experimentally with a variety of single/multilayered columns. A number of adsorbents were tested as the H_2O-removal prelayer in combination with zeolite 13X as the CO_2-capture layer. The axial concentration and thermal profiles were examined to interpret the water front. Additional efforts were paid to the determination of purge-to-feed ratio and the optimization of layer ratios. Principal experimental results were further compared with our supplemental computer simulations.

Experimental Work

As shown in Figure 1, we adopted a simple three-step cycle for the VSA process: adsorption (45 s), countercurrent evacuation (variable time), and repressurization (3 s). The evaluation criteria, namely CO_2 recovery, purity, and productivity were defined as usual.[6] The operating conditions, layering patterns, and the performance of all the experiments are summarized in Table 1.

The VSA apparatus of this work was an upgraded version of the one used in our previous studies,[6] with 11 thermocouples (tagged as T_1, $T_2, \ldots, T_{11}$) measuring the column axial temperatures. The corresponding locations of these thermocouples from bottom to top of the column were $Z = 0.035$ (T_1), 0.105 (T_2), 0.175 (T_3), 0.246 (T_4), 0.316 (T_5), 0.386 (T_6), 0.456 (T_7), 0.526 (T_8), 0.679 (T_9), 0.832 (T_{10}), 0.984 (T_{11}), respectively, where Z is the dimensionless length based on 570 cm of the total adsorbent packed column.

Table 1. Summary of Experimental Operating Conditions and Results for CO_2/H_2O VSA with Single and Layered Columns, respectively

Run No.	T (°C)	Feed Conditions	Layer Content and Dimensionless Length Z			Feed y_i (%)		Flow Rate (LPM[a])	P_{high} (kPa)	P_{low} (kPa)	Desorp. Time (s)	Rec. CO_2 (%)	Pur. CO_2 (%)	Productivity ($kgCO_2$/h/L Adsorbent)
			First layer	Second layer	Third layer	CO_2	H_2O							
1	20	Dry CO_2 in air	13X, Z(0,1)	–	–	11.2	–	66	116	2.9	112	82	73.6	0.317
2	30	Dry CO_2 in air	13X, Z(0,1)	–	–	10.7	–	71	120	2.3	112	78.5	69	0.287
3	30	Wet 53.2% RH	13X, Z(0,1)	–	–	10	1.89	68	120	2.5	112	73.4	53	0.240
4	30	Wet 76.6% RH	13X, Z(0,1)	–	–	10	2.73	68	119	2.6	112	71.7	57	0.235
5	30	Wet 96.8% RH	13X, Z(0,1)	–	–	11	3.48	68	118	2.9	112	68.2	58.5	0.246
6	30	Wet 94.6% RH	13X, Z(0,1)	–	–	12	3.4	63	118	3.9	112	60.4	72	0.220
7	30	Wet 97.4% RH 112 s desorp.	13X, Z(0,1)	–	–	10.7	3.5	69	119	3.2	112	68	59	0.242
8	30	Wet 97.4% RH 100 s desorp.	13X, Z(0,1)	–	–	10.7	3.5	68.7	118	3.8	100	61	57	0.234
9	30	Wet 97.4% RH 80 s desorp.	13X, Z(0,1)	–	–	10.7	3.5	66.8	118	4.2	80	39	47	0.107
10	50	Wet 41.5% RH	13X, Z(0,1)	–	–	12	4.3	67.5	119	1.3	112	<4.6	39	<0.018
11	30	Dry CO_2 in air, 112 s desorp.	CDX, Z(0, 0.266]	13X, Z(0.266, 1)	–	10.7	–	70	118	2.3	112	78.5	68.5	0.183
12	30	Wet 97.4% RH, 112 s desorp.	CDX, Z(0, 0.266]	13X, Z(0.266, 1)	–	10.7	3.48	69.5	118	2.89	112	76.9	67	0.178
13	30	Wet 97.4% RH, 100 s desorp.	CDX, Z(0, 0.266]	13X, Z(0.266, 1)	–	10.7	3.5	68	118	3.73	100	65.5	63.7	0.160
14	30	Wet 97.4% RH, 80 s desorp.	CDX, Z(0, 0.266]	13X, Z(0.266, 1)	–	10.7	3.48	68	118	4.47	80	58.3	62	0.165
15	30	Dry CO_2 in air, 112 s desorp.	F200, Z(0, 0.227]	13X, Z(0.227, 1)	–	10.4	–	68	118	2.7	112	71.6	70	0.158
16	30	Wet 97.4% RH, 112 s desorp.	F200, Z(0, 0.227]	13X, Z(0.227, 1)	–	10.7	3.5	67	117.5	2.73	112	78.2	65	0.176
17	30	Wet 97.4% RH, 100 s desorp.	F200, Z(0, 0.227]	13X, Z(0.227, 1)	–	10.5	3.48	68	118	3.1	100	69.4	66.5	0.167
18	30	Wet 97.4% RH, 80 s desorp.	F200, Z(0, 0.227]	13X, Z(0.227, 1)	–	10.4	3.48	68.5	118.5	3.8	80	58.3	65	0.162
19	50	Wet 41.4% RH	F200, Z(0, 0.24]	CDX, Z(0.24, 0.52]	13X, Z(0.52, 1)	12	4.3	67.5	118	2.7	112	68.7	64.7	0.170
20	50	Wet 55.0% RH	F200, Z(0, 0.24]	CDX, Z(0.24, 0.52]	13X, Z(0.52, 1)	10.7	5.8	68.4	118.5	2.8	112	60.8	60.5	0.138
21	50	Wet 81.7% RH	F200, Z(0, 0.24]	CDX, Z(0.24, 0.52]	13X, Z(0.52, 1)	10.7	8.5	67.5	117.5	3.1	112	58.2	52.4	0.128
22	30	Dry CO_2 in air	F200, Z(0, 0.24]	CDX, Z(0.24, 0.52]	13X, Z(0.52, 1)	10.7	–	69	117.5	2.3	112	69.1	71.9	0.158

[a] Liter per minute as measured.

Table 2. Summary of Simulation Conditions and Results of Different Runs for CO_2/H_2O VSA with Single and Layered Columns, Respectively

Run No.	T (°C)	Simulation Conditions	Layer Content and Dimensionless Length Z		Feed y_i (%)		Flow Rate (LPM[a])	P_{high} (kPa)	P_{low} (kPa)	Desorp. Time (s)	Rec. CO_2 (%)	Pur. CO_2 (%)	Productivity ($kgCO_2$/h/L Adsorbent)	Power[b] (kW/$TPDCO_2$)
			First layer	Second layer	CO_2	H_2O								
S1	30	Wet 94.6% RH	F200, Z(0, 0.227]	13X, Z (0.227, 1)	10.7	3.4	68	118	1.0	112	77.6	74.8	0.200	11.7
S2	30	Wet 94.6% RH	F200, Z(0, 0.227]	13X, Z (0.227, 1)	10.7	3.4	68	118	3.0	112	65.4	73.1	0.169	9.8
S3	30	Wet 94.6% RH	F200, Z(0, 0.227]	13X, Z (0.227, 1)	10.7	3.4	68	118	5.0	112	48.5	69.3	0.126	9.6
S4	30	Wet 94.6% RH	F200, Z(0, 0.227]	13X, Z (0.227, 1)	0	2.73	68	118	3.0	112	0	0	0	–
S5	30	Wet 94.6% RH	F200, Z(0, 0.227]	13X, Z (0.227, 1)	35.0	3.48	68	118	3.0	112	54.0	93.6	0.4608	5.66
S6	30	Dry 0% RH	F200, Z(0, 0.227]	13X, Z (0.227, 1)	10.7	0	68	118	3.0	112	64.0	72.3	0.166	8.0
S7	30	Wet 38.7% RH	F200, Z(0, 0.227]	13X, Z (0.227, 1)	10.7	1.39	68	118	3.0	112	64.5	72.5	0.167	8.8
S8	30	Wet 58.1% RH	F200, Z(0, 0.227]	13X, Z (0.227, 1)	10.7	2.09	68	118	3.0	112	64.8	72.7	0.168	9.1
S9	30	Wet 77.5% RH	F200, Z(0, 0.227]	13X, Z (0.227, 1)	10.7	2.78	68	118	3.0	112	65.1	72.9	0.169	9.5

[a] Liter per minute as measured.
[b] TPD denotes ton-per-day.

Another 11 gas sample ports were added at each of the thermocouple positions (Supporting Information Figure S1). The system was insulated by 1-cm thick ceramic fiber cloth, 1-cm thick nitrile rubber, and aluminium foil. A water bubbler tank was used as the humidifier with an internal heater to control the temperature. Air was humidified by adjusting the bubbler temperature and pressure, blended with pure CO_2 to reach the required composition, and then transported to the buffer tank. The temperature and the partial pressure of the humid gases were analyzed by an *in situ* water sensor (HMT330, VAISALA, Finland, ±0.05% full scale). All experimental control and data acquisition were managed by the Advantech® system.

Apart from the single-adsorbent layer experiments, a double-layer and a triple-layer pattern were used for the column configuration (Supporting Information Figure S1). The double-layered column used a prelayer at the bottom (inlet) of the column for water removal and a 13X main layer for CO_2 capture. Two commercial alumina desiccants were tested for the prelayer namely F200 (Engelhard, US) and Selexsorb® CDX adsorbent (CDX; BASF, Germany). For comparison purposes, the same mass of water adsorbent (200 g) was placed in the prelayer and the remainder of the bed was filled with 13X zeolite in each case. Detailed physical properties of the adsorbents and the column are provided in Supporting Information Tables S1 and S2. The triple-layered column consisting of F200/CDX/13X was designed for high humidity feeds (~8% v/v water), with F200 to remove bulk water, CDX to remove trace water and capture a part of the CO_2, and eventually 13X to capture the majority of the CO_2. VSA experiments with dry feed gases were carried out as base runs prior to the wet runs.

Computer Simulation

The VSA processes were simulated with our in-house adsorption simulator to compare with the major experimental findings and investigate some process conditions that were not experimentaly available. Developed by Webley and He[33] with FORTRAN, this well-tested simulator uses the numerical solution of the coupled mass and energy balance equations together with the viscous flow/dusty gas model to represent adsorption kinetics. The numerical method uses a solution-adaptive finite volume method with appropriate flux-limiters and is based on the additional assumptions (see Supporting Information). All the simulation conditions and results are summarized in Table 2.

Results and Discussion

Effect of purge-to-feed ratio

Purge-to-feed ratio (P/F) is a very important parameter in controlling the product purity in PSA processes.[15,34–37] A purge step is normally conducted by adding a portion of the light product component into the column counter-currently (i.e., from the product end) to push the concentration front of the heavy impurity components backward to "clean" the bed and avoid premature breakthrough of the heavy components on the subsequent adsorption step.[34–38] P/F is generally defined as the ratio of the moles of light component used in purge step to that used in the feed step regardless of step time.[37,39] LeVan[40] and, Pigorini and LeVan[32] defined a critical volumetric purge-to-feed ratio to characterize the minimum P/F required to keep the adsorbate contained within the

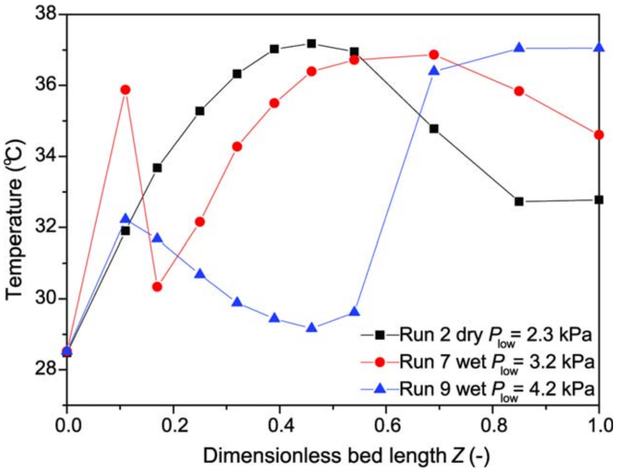

Figure 2. Axial temperature profile at the end of the adsorption step depending on dry/wet feed and vacuum pressure at 30°C of Run 2, 7, and 9.

[Color figure can be viewed in the online issue, which is available at wileyonlinelibrary.com.]

bed at cyclic steady state (CSS). A PSA process often uses a large amount of external gases, either from the product line/tank, or a different gas to purge the column. The gases removed during the purge step are usually disposed of as dilutes waste products. However, it is very different for CO_2VSA with humid feed, in which the principal step is to recover high purity heavy components, namely CO_2 and water, and regeneration of the bed is by evacuation rather than by "external" purge. As water is adsorbed at the bottom of the bed due to its highly favorable isotherm shape, all the remaining components lighter than water (CO_2 and air) are adsorbed in the upper layers. During the countercurrent evacuation step, the desorbed lighter components, essentially a dry gas stream, will facilitate the desorption of water by means of a so-called "internal purge" effect.[41] Therefore, the rapid change of the vacuum pressure must be taken into account in determining the forwards and backwards propagation of the water concentration front during the adsorption and desorption steps, respectively, at CSS. By reviewing the linear driving force model (see Supporting Information),[42,43] we adopted the volumetric P/F ratio for effective characterization of the repeated adsorption/desorption of water vapor in the presence of internal purge in VSA.

Case Study: VSA with Single-Layered Bed. We define the volumetric P/F ratio as the total volume of all the counter-current flow (evacuation from the bottom and backfill from the top) against the total volume of the gas flow fed to the bottom of the column. This implies both Step 2 and Step 3 are purge and only Step 1 is feed (Figure 1). However, the contribution of the repressurization step in this work can be ignored due to its small quantity (<0.5% of the feed amount).

We use the single-layered CO_2/H_2O VSA system as an example. As the cycle proceeds after startup, the length of the water loaded zone, Z_w evolves slowly to a constant value at CSS when there is no net accumulation of water in the bed. This Z_w can be determined experimentally by using the "cold spot" technique.[6,41] Corresponding to the position of the water front at a local temperature minimum, the "cold spot" is caused by the regenerative heat exchange effect due to the abrupt change of adsorption properties in the water contaminated layer and the main CO_2 layer. The "cold spot" is visible in runs with wet gas (Run 7 and 9) while absent in the case of dry feed (Run 2), as can be observed from the axial temperature profiles (Figure 2). We were able to identify and plot this cold spot position Z_w against the volumetric P/F ratio. As shown in Figure 3a, Z_w increases exponentially with the decrease of P/F ratio. In the region of $P/F > 1.7$, water front is confined to the bottom of the bed ($Z_w \approx 0.2$), indicating further withdrawal of the water front may not be worthy as it requires a rather prolonged evacuation time due to the highly favorable equilibrium isotherm of water in 13X. However, in the region of $P/F < 1.7$, a small reduction of P/F will lead to a sudden increase of Z_w, because the migration of water front will "nibble" at the dry 13X layer used for CO_2 adsorption, and in return reduce the amount of internal purge, provided by the desorbed CO_2. In this region, CO_2 productivity, recovery, and purity fall sharply with the decrease of P/F (Figure 3b). Thus, when P/F is below a certain lower limit which we define as the critical P/F ratio[32,40]—approximately 1.7 in this case, water front becomes unbounded, tends to penetrate the column, and eventually destroys the CO_2 capture ability of the column irreversibly. Run 10 provides an example of such "creeping death." In this run, the feed water concentration was increased to 4.3% v/v, the highest humidity among all the 10 runs using a single-layered column. Eventually a water concentration of 740 ppmv was detected in the gas stream from the top of the column and no cold spot was observed, indicating penetration of the entire column by water vapor with a corresponding $Z_w \geq 1$ (Figure 3a) in this case. The column has lost its capacity to capture CO_2 as reflected by a very low CO_2 recovery (<4.6%). It should be noted that at the end of evacuation the pressure was only 1.3 kPa—the deepest vacuum in all the runs but also the highest in terms of water partial pressure. That means no CO_2 was recovered from the column and the power of the pump was solely used for removing the water vapor from the column, while the P/F ratio was as low as 0.69. Therefore, it is clear that CO_2 capture by VSA with a single-layered 13X column is vulnerable to the intrusion of water vapor. Any disturbance of P/F below its critical value may cause breakthrough of H_2O and consequently a process failure even at a deep final vacuum (e.g., < 1.3 kPa in Run 10). Once the VSA fails, one may have to reload the column with new adsorbents, as the regeneration of wet 13X zeolite needs an elevated temperature. Nevertheless, the process failure could be avoided by operating the VSA above its critical P/F ratio with some safety margin, or by adding a prelayer specifically for water removal and protection of the main CO_2 adsorbing layer.

Effect of layering pattern

Double Layered VSA. The desired product in our VSA process is high purity CO_2. However, as a heavy component, water vapor must be prevented from breaking through the column and it is, therefore, recovered as a by-product. During the adsorption step, water is adsorbed by the bottom layer, that is, the prelayer of the column, and CO_2 is adsorbed by the 13X main layer. The light components N_2 and O_2 quickly penetrate the column into the waste line. Owning to the large enthalpy changes of the heavy components,[44] one can readily use thermal profiles to infer H_2O and CO_2 mass transfer fronts. Herein, we chose activated

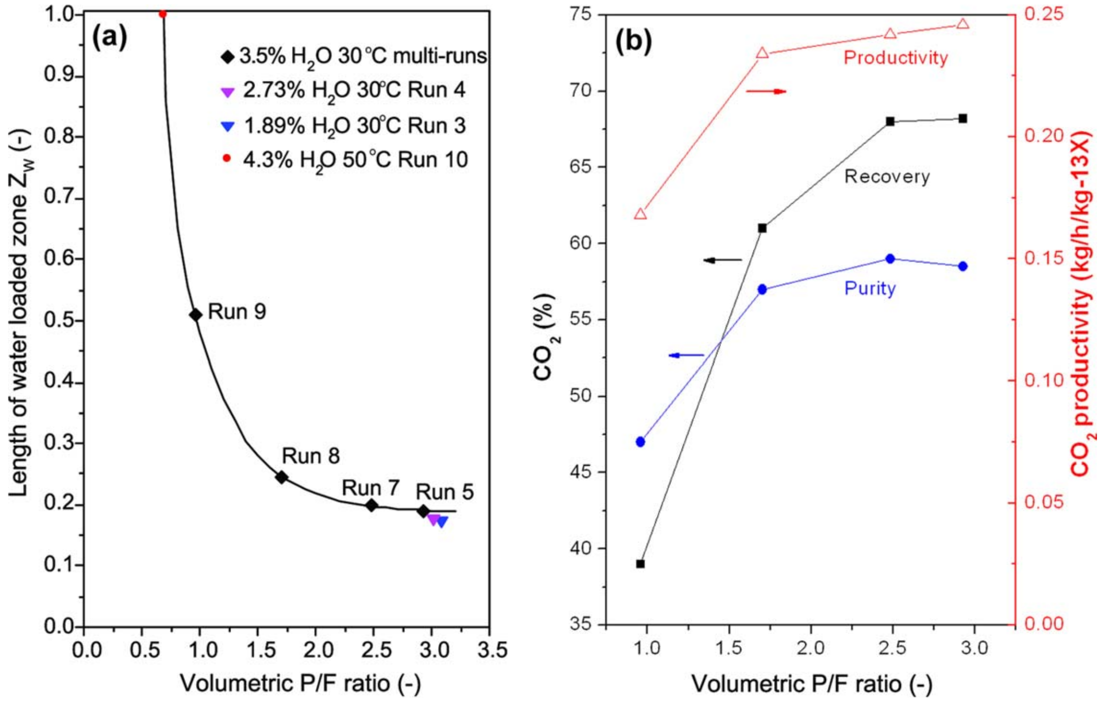

Figure 3. (a) Dependence of water loaded length on volumetric purge-to-feed ratio at CSS of single-layer 13X VSA processes.

Note: vacuum level decreases in the order of Run 5, 7, 8, 9, and 10. (b) Dependence of CO_2 productivity, purity, and recovery on volumetric purge-to-feed ratio at CSS of single-layer 13X VSA processes with 3.5% water feed at 30°C. [Color figure can be viewed in the online issue, which is available at wileyonlinelibrary.com.]

alumina CDX and F200, respectively, as the prelayers because of their wide application in adsorption based driers.[15,45,46]

Figure 4 shows the complete temperature profiles of the CDX/13X double-layered column in the form of a "heat map," with dry and wet feed conditions, respectively. The heat map is a two-dimensional (2-D) evolution of the axial thermal profiles during the VSA cycle. For additional clarity, several axial profile "snapshots" were plotted in the form of conventional 2D curves (Supporting Information Figure S2) to help understand the shape and the transmission trajectory of the thermal waves. In the case of dry CO_2 feed (Figure 4a), the amplitude of the temperature swing in the upper part of the column ($Z = 0.7$) was more pronounced than that below the layer interface due to the higher working capacity of CO_2 on 13X than on CDX. Moreover, during desorption stage ($45\ s < t < 157\ s$), the location of the coldest point in the column—between T_4 ($Z = 0.246$) and T_5 ($Z = 0.316$) at 160 s, corresponds to the location of the layer interface ($Z = 0.266$), indicative of the discontinuity of the heat of adsorption in the bed (e.g., for CO_2 adsorption, $\Delta H_{CDX} \neq \Delta H_{13X}$) and the formation of the cold spot even in dry gas feed (Supporting Information Figure S2a).

With wet CO_2 feed (Figure 4b), there were two temperature waves propagating along the column. The broad temperature wave was attributed to the adsorption heat of CO_2 in the 13X layer. The maxima of the wave was controlled to the position of T_9 ($Z = 0.679$) with some gap to the column outlet, in order to retain the heat of adsorption within the column for providing energy to the subsequent desorption step and also improving the CO_2 product purity. The other short and sharp temperature wave characterized by T_1 ($Z = 0.035$), T_2 ($Z = 0.105$), and T_3 ($Z = 0.175$) was caused by water adsorption in the prelayer. We can see a distinct boundary between the two cold zones at the end of desorption step ($130\ s < t < 157\ s$), highlighted with a horizontal dashed line in Figure 4b. However, the thermal front of water reached T_3 ($Z = 0.175$) only, suggesting T_4 ($Z = 0.246$)—the last thermocouple in the prelayer, was still dry at CSS. The temperature profile also showed a valley around T_4 (highlighted with a dashed square in Figure 4b), indicating the existence of a short zone of dry alumina CDX, which is further evidenced by the gas-phase water concentration in Figure 5.

However, in the case of wet feed with a shorter desorption time of 80 s (Figure 4c, Run 14), the temperature swing in the 13X layer was less pronounced than that in the previous cases, because of the reduced working capacity of CO_2 with narrower pressure window. We found in Run 14 that the H_2O thermal wave developed further into the prelayer and the wave amplitude was also greater than that of CO_2 in the 13X main layer because of the higher heat of adsorption of H_2O on alumina. The valley between the two thermal waves (Figure 4c) was much squashed with the increase of water loaded zone but the water front was still retained within the activated alumina prelayer (Figure 5). One of the major findings from this part is that the overall performance of a double-layered VSA is superior to that using single 13X layer at wet feed conditions. Even under very harsh conditions with saturated humidity and 80 s short evacuation, our single-column VSA process using F200/13X double-layered packing could achieve a reasonable CO_2 recovery, purity, and productivity of 58.3%, 65%, and 0.162 kg CO_2/h/L-adsorbent, respectively, whereas the corresponding performance of the VSA with single-layered 13X packing was quite poor, with only 39%, 47%, and 0.107 kg CO_2/h/L-adsorbent, respectively.

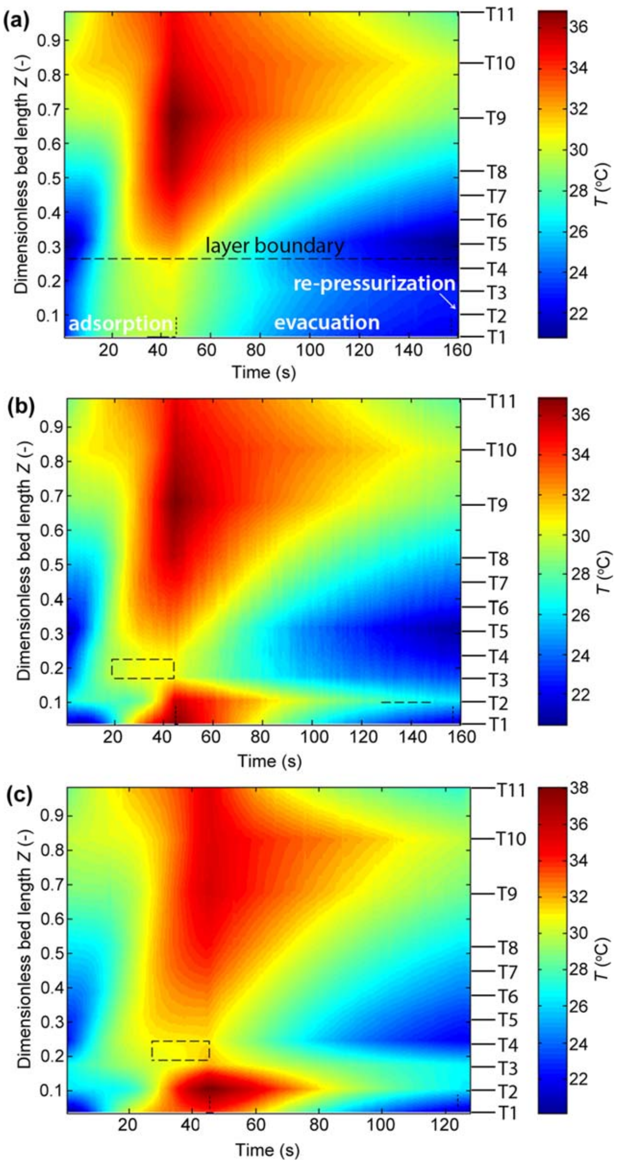

Figure 4. Axial thermal profiles of a complete cycle at CSS for CDX/13X double-layered bed during VSA at 30°C, (a) dry CO_2 feed in Run 11, (b) saturated CO_2 feed in Run 12, and (c) saturated CO_2 feed with shortened desorption time of 80 s in Run 14.

The dashed lines are for guidance. Vertical dashed lines represent boundaries between cycle steps. [Color figure can be viewed in the online issue, which is available at wileyonlinelibrary.com.]

Triple-Layered VSA. Postcombustion flue gases are saturated at the operating temperature (higher than the above cases) of the washing tower and then remain saturated in the downstream feed lines. Any abrupt variation of environmental temperature will affect the water content of the "washed" flue gases fed to the carbon capture unit. Therefore, there is a need to design a robust layered column working effectively over a wide range of water content. For example, a longer prelayer can be used to completely remove H_2O and ensure the gas entering 13X main layer is absolutely dry. However, this will cause excessive unused prelayer for the purpose of accommodating variable feed humidities, and reduce the overall CO_2 capture performance.

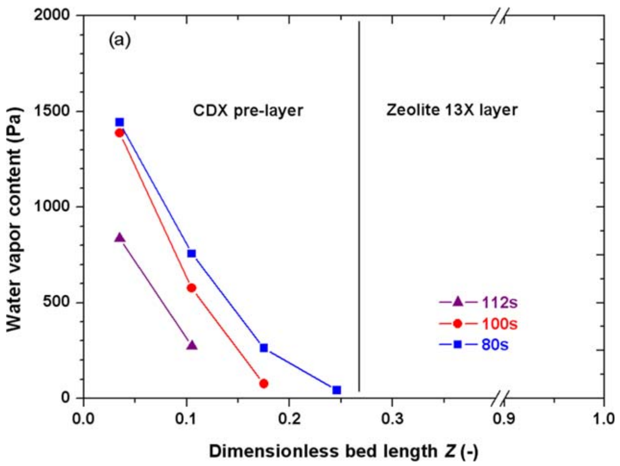

Figure 5. Water concentration profile in the gas phase in the double-layered CDX/13X VSA column at the end of the adsorption step for cycles with different desorption time: 112 s (Run 12), 100 s (Run 13), and 80 s (Run 14).

The dashed line represents the interface between the two layers. [Color figure can be viewed in the online issue, which is available at wileyonlinelibrary.com.]

To overcome the above difficulty, one strategy is to add a middle layer of adsorbent with reasonable working capacity for both CO_2 and H_2O, located in between the H_2O prelayer and CO_2 main layer. This middle layer can increase the robustness and flexibility of the process against variable feed compositions. Alumina CDX is a particularly good candidate for this middle layer, because CDX shows doubled CO_2 capacity compared with F200 and similar quasilinear or Brunauer–Emmett–Teller (BET)-type water isotherm, exhibiting large working capacities under VSA conditions in this study (Supporting Information Figure S3). Conversely, by comparing the CO_2 capture performance of double-layered VSA processes using activated alumina CDX (Run 11–14) with that using F200 (Run 15–18), we can conclude F200 is marginly better than CDX as a prelayer at wet feed conditions, whereas CDX performs better at dry feed conditions owing to its larger CO_2 capacity.

Here, we used a F200/CDX/13X triple-layered column to treat flue gases with high water content up to 8.5% v/v. The layering ratio was preset as 0.24:0.28:0.48 (Supporting Information Figure S1b). In the case of dry CO_2 feed (Figure 6a), the average temperature change from the end of the adsorption step to the end of the desorption step is 3, 8, and 12°C in the F200, CDX, and 13X layers, respectively, consistent with the order of CO_2 working capacity on these three adsorbents. Two cold spots can be observed on the two interfaces, namely F200/CDX and CDX/13X, as a result of the discontinuity of the heat of adsorption from one layer to another. The overall performance of dry CO_2 feed (Run 22) was 69.1% recovery, 71.5% purity, and 0.158 kg CO_2/h/L-adsorbent productivity, slightly less but still comparable to that in a single layered 13X column.

In the case of wet CO_2 feed, the largest temperature change of up to 22°C occurred in the first F200 prelayer, due to the large heat of adsorption of H_2O (Figure 6b). Meanwhile, as a result of reduced vacuum level in the presence of water, both the temperature changes of the CDX

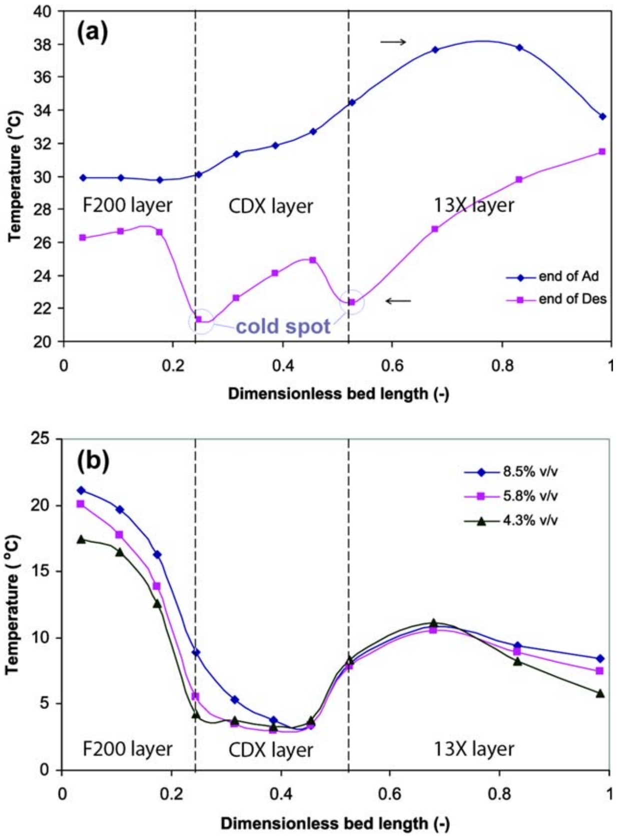

Figure 6. (a) Thermal profiles in triple-layered column with dry CO_2 feed at CSS in Run 22 at the end of adsorption and desorption step, respectively.

(b) Temperature changes (ΔT) in the triple-layered columns measured by individual thermocouples in a single cycle at CSS for wet CO_2 feed at different water concentrations: 4.3% v/v (Run 19), 5.8% v/v (Run 20), and 8.5% v/v (Run 21). The layer interface of F200/CDX is at $Z = 0.24$ and CDX/13X interface at $Z = 0.52$. Arrows represent gas flow directions. [Color figure can be viewed in the online issue, which is available at wileyonlinelibrary.com.]

middle layer and the 13X main layer decreased in comparison with the run of dry feed (Run 22). As mentioned earlier, the relative intensity of temperature excursion ΔT reflects the adsorbed amount. An examination of Figure 6b shows that ΔT at the prelayer increases with increasing feed water concentration; and correspondingly the front of the ΔT curve proceeds from the F200/CDX interface (Run 19) further into the CDX middle layer (Run 20) and eventually reaches the layer interface of CDX/13X (Run 21). In the case of the highest feed humidity of 8.5% v/v (Run 21), a reasonable carbon capture performance was achieved: 58.2% recovery, 52.4% purity, and 0.128 kg CO_2/h/L-adsorbent productivity, with such a single column triple-layered VSA and a simple three-step cycle. The employment of multicolumns and full process steps, such as product purge and pressure equalization, can further improve the overall performance.

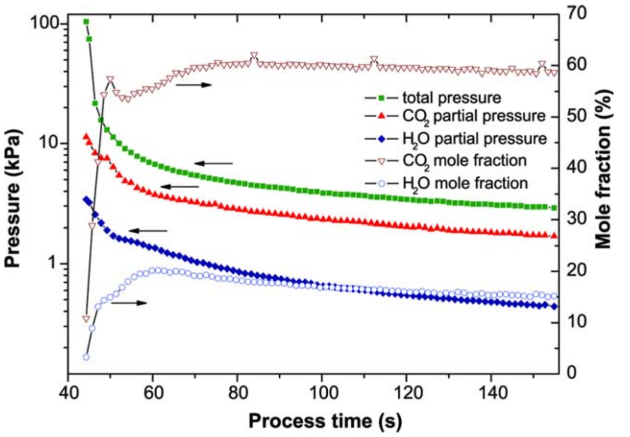

Figure 7. Pump down curve in terms of partial pressure and mole fraction during the 112 s evacuation step of CO_2/H_2O VSA (Run 12).

[Color figure can be viewed in the online issue, which is available at wileyonlinelibrary.com.]

Effect of desorption time/vacuum level

During the evacuation step, water vapor and CO_2 are desorbed from the column along with the weakly adsorbed N_2 and O_2 and gases from the void spaces, where CO_2 and H_2O mole fractions increase with decreasing partial pressures, for example, Run 12 with CDX/13X double-layered column. At the end of the desorption step, the CO_2 partial pressure reaches 1.70 kPa and the H_2O partial pressure reaches 0.44 kPa (Figure 7). It must be pointed out that the CO_2 concentration of the product stream increased after leaving the vacuum pump, because water vapor was condensed and trapped in the vacuum pump. In field applications, this water would be recovered by the liquid ring vacuum pump for other uses in a power plant.

Limited by the fixed feed conditions such as CO_2 concentration, flow rate, pressure, and step time in some of our experiments, the major parameters influencing the desorption are the evacuation time and consequently, the final vacuum pressure. Longer evacuation time provides a deeper vacuum level and enhanced CO_2 desorption as expected. As a result, the bed is cleaner and gives higher working capacity for CO_2 and other weakly adsorbed gases (N_2 and O_2), which will subsequently contribute to larger amount of internal purge. Meanwhile, deeper vacuum level also means a larger volume of internal purge for the same amount of desorbed gas. This combined effect increases the P/F ratio (for fixed feed) and retains the water front in the prelayer. The water front moved further into the column as evacuation time decreased. In the worst case—80 s desorption, water already reached T_4 ($Z = 0.246$), very close to the layering interface of CDX/13X. Consequently, the CO_2 product recovery and purity declined with further decrease of evacuation time and vacuum level (Figure 8a).

Using computer simulations, we can arbitrarily reduce the vacuum level while keeping the evacuation time constant, in order to investigate the separate effect of vacuum level. In Figure 8b, the wedge-shaped concentration wave of water vapor moved deeper into the column when the evacuation pressure was raised from 1 to 3 kPa. At a fixed feed concentration, the starting point of the concentration wave remained constant regardless of desorption conditions and only the slope of the wave decreased with the progression of the front. When the evacuation pressure was above 5 kPa, the front of water vapor became unbounded and tended to break

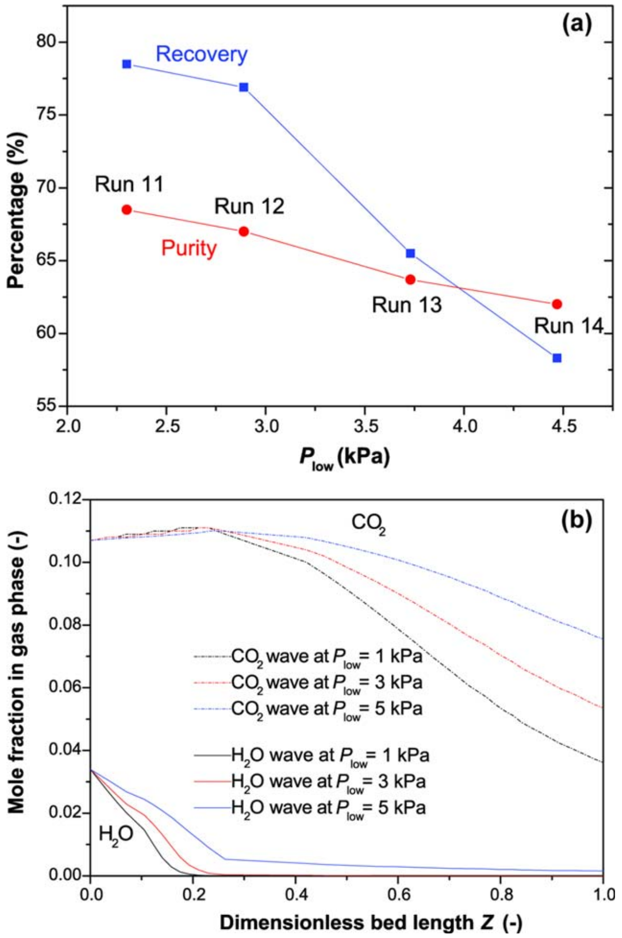

Figure 8. (a) CO_2 product purity and recovery for dry (Run 11) and wet CO_2 VSA (Run 12–14) with different desorption times and corresponding final vacuum pressures.

(b) Gas-phase water and CO_2 distribution in the column at the end of the adsorption step, of simulation Run S1, S2, and S3. The feed gas contains 3.4% water and 10.7% CO_2. [Color figure can be viewed in the online issue, which is available at wileyonlinelibrary.com.]

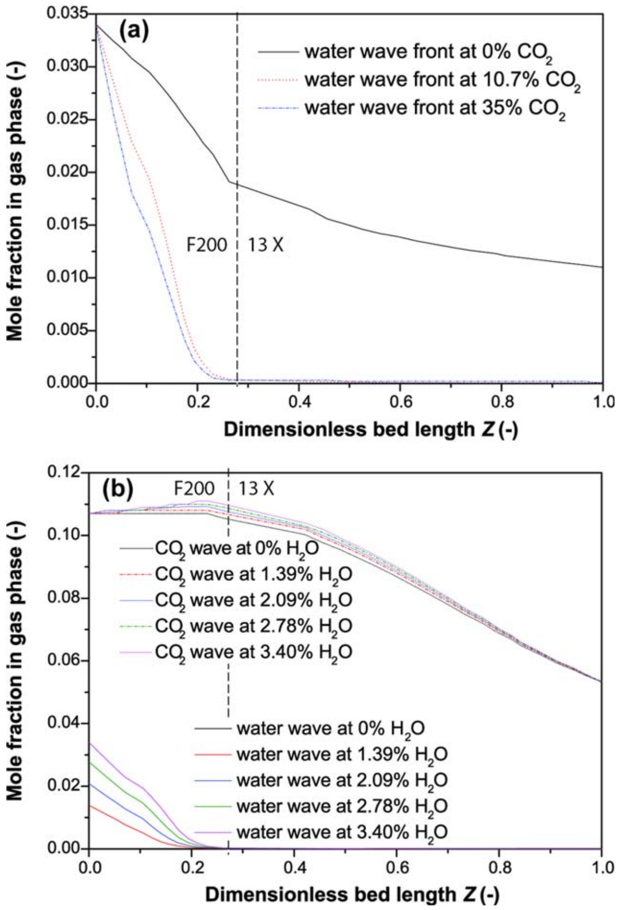

Figure 9. (a) Water wave in gas phase at various feed CO_2 concentration levels: 0% in S4, 10.7% in Run S2, and 35% in S5.

(b) Water and CO_2 wave in gas phase at various feed H_2O concentration levels: 0% in Run S6, 1.39% in S7, 2.09% in S8, 2.78% in S9, 3.4% in S2. [Color figure can be viewed in the online issue, which is available at wileyonlinelibrary.com.]

through the entire column. Clearly, a lower vacuum level (higher P_{Low}) leads to a smaller P/F ratio and consequently, a longer water loaded zone.

Effect of feed concentration

The feed concentration of the main adsorptives can greatly affect the feed and purge terms of the P/F ratio, and was investigated by our computer simulation (Table 2).

Reviewing the purge function, the total volume of purge gas V_P is the summation of the volume of desorbed CO_2, air, and H_2O, expressed as follows

$$V_P = V_{P,CO_2} + V_{P,air} + V_{P,H_2O} \tag{1}$$

where the main adsorptive CO_2 takes up the majority of the total purge, and the carrier gas air and the secondary adsorptive H_2O take up the remainder.

The total volume of feed gas V_F can be described similarly

$$V_F = V_{F,CO_2} + V_{F,air} + V_{F,H_2O} \tag{2}$$

where the majority is the carrier gas air, the second largest fraction is CO_2, and the smallest fraction is H_2O. The change of feed composition will not affect the total volume of feed gas V_F, as the volumetric flow rate of the feed is constant, but it will affect V_P. By increasing the concentration of CO_2 in the feed stream, the volume of desorbed CO_2 increases accordingly, and the absolute value of V_P will increase. Therefore, the P/F ratio (V_P/V_F) will become larger. From Figure 9a, we can see that with zero CO_2 in feed—nearly zero internal purge, water broke through the column immediately. With 10.7% CO_2 in feed, the concentration of water showed a repeated identical linear wave at the end of adsorption step of each cycle (not plotted) from cycle 100 to cycle 500, suggesting a stabilized front at CSS. Increase of CO_2 feed concentration from 10.7 to 35% increased the P/F ratio. However, the water front retreated only slightly at higher CO_2 feed (Figure 9a), which is consistant with our above experimental findings that further withdrawal of the water front is costly and less effective above the critical P/F ratio.

Here, the major constraint is that the recovery of water must be strictly 100% to prevent any breakthrough at CSS. Increasing water concentration in the feed will give higher V_{P,H_2O} in Eq. 1. However, the net contribution to V_P can be neutral or most likely, negative, considering that the amount

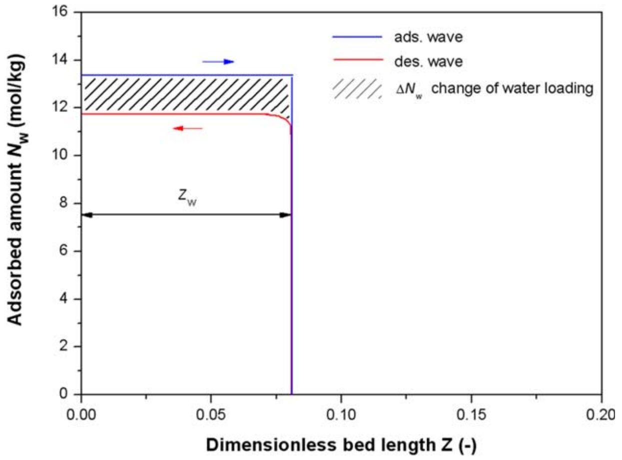

Figure 10. Anticipated solid phase concentration wave of water at the end of adsorption and desorption in Run 5.

[Color figure can be viewed in the online issue, which is available at wileyonlinelibrary.com.]

of CO_2 recovered will decrease due to competitive adsorption of water. In Figure 9b, when the water concentration increased from 1.39 to 3.4%, the location of the water front only moved 20% forward, whereas the height of the water concentation wave was more than doubled. This indicates the increased amount of feed water concentration can be captured mainly by expanding the working capacity of the water occupied adsorbent layer, rather than further intruding the dry column layers proportionally.

Determination of water loaded zone

The ultimate aim of this work is to understand the penetration depth and distribution profile of water vapor inside the adsorption column and the subsequent effect on the carbon capture performance in the presence of water and, determine the forwards and backwards propagation of the water concentration front during the adsorption and desorption steps at CSS. The model developed below achieves these goals without undue complexity.

General Analytical Approach. At CSS, the amount of water fed into the bed equals the amount of water recovered by evacuation. This mass balance condition can be expressed as

$$\int_0^{Z_w} (N_{w.i}-N_{w.f}) \frac{\pi D_{in}^2 \rho_b L}{4} dZ = \int_0^{t_f} \frac{v_F P_w}{RT} dt \tag{3}$$

where the subscripts w, i, f, and F denote water component, initial, final and feed conditions, respectively. The right-hand side is the total water fed to the column during the feed step. Note that N_w is a function of the local temperature and partial pressure of water. To solve Eq. 3, an axial distribution pattern of N_w is indispensable, which can be obtained by either experimental measurement or computer simulation.

An analytical solution to this type of problem was attempted by Wilson et al.[41] in the case of O_2VSA, with an approach similar to that by LeVan,[40] by assuming the adsorption front as a shock wave and the desorption front as a simple wave.[47] In that work, the velocity of the water front was characterized by a mass balance

$$\frac{dz}{dt} = \frac{v}{\varepsilon_t \left(1 + \frac{\rho_b RT}{\varepsilon_t} \frac{dN_w}{dP_w}\right)} \tag{4}$$

To locate the water loading profile at the end of the evacuation (and/or purge) step, an estimated length of water loaded zone is required and the solution to Eq. 4 is necessary. However, this approach heavily depends on detailed experimental or computer simulation data to determine the bed pressure as a function of time and to calculate the average gas velocity v and, it cannot provide straightforward expression of the minimum water penetration depth. Therefore, if it is solely for the purpose of determining the water front, the above technique would be no more accurate or convenient than the "cold spot" method or more sophisticated magnetic resonance imaging.[48,49]

As measurement of temperature change along the adsorption column is more convenient than that of concentration, by calculating the maximum temperature excursion at each thermocouple position along the column in a complete cycle at CSS, it is possible to estimate the dynamic working capacity of the adsorbate under adiabatic conditions during a single VSA cycle, that is, $N_{\text{end of adsorption}} - N_{\text{end of desorption}}$. Assuming the axial convection is negligible while ignoring gas-phase accumulation[50] we get

$$\frac{dT}{dN} = \frac{\Delta H}{C_s} \tag{5}$$

which means the amount of adsorbate recovered by each node of the column in a cycle is proportional to the corresponding temperature change.

In the following parts, we demonstrate how to calculate the adiabatic working capacity by using the temperature profile. Once $N_{w.i}-N_{w.f}$ is determined, the penetration depth of water Z_w in the column can be resolved immediately from Eq. 3. Two typical patterns of water concentration wave will be investigated to understand the axial distribution of N_w and ultimately, to determine the length of water loaded zone Z_w.

Case I: Shock Wave Front and Adiabatic Conditions. As previously noted by LeVan[40] and Wilson et al.,[41] the adsorption front of water propagates as a shock wave because of the highly favorable adsorption isotherm of water on zeolite 13X (Supporting Information Figure S3b). Although the real wave front may be slightly dispersed, the assumption of a shock wave still remains a good approximation for water front in columns packed with materials having strongly favorable isotherms such as water on 13X.

The temperature change can be determined by calculating the difference between the temperatures at the end of adsorption and at the end of desorption steps. It was observed that the temperature change in the water loaded zone ($\Delta T = 9.1°C$ at T_2 ($Z = 0.105$) position and $\Delta T = 10.3°C$ at T_3 ($Z = 0.175$)) was almost even axially for Run 5, suggesting the amount of water removed by each node (axial working capacity ΔN_Z) in a single cycle was of similar quantity. Therefore, we can anticipate the concentration profile of water remains in a shock wave during desorption, rather than a dispersive wave. However, the ratio of countercurrent purge amount (mainly by internal N_2) to the amount of H_2O desorbed is around 10:4 in our CO_2VSA, approximately 8 times smaller than that in O_2VSA (~80:4). Practically, in a PSA process, the purge amount can be increased by adding extra external purge gases (e.g., product purge). In this work,

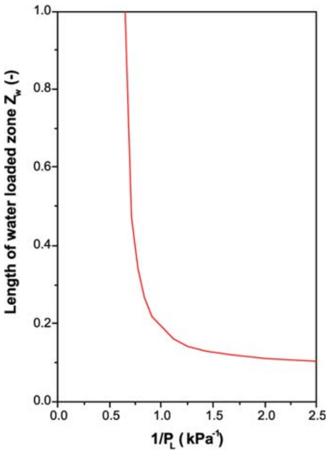

Figure 11. Dependence of water loaded zone on the reciprocal of water partial pressure P_{L,H_2O} in 13X single-layer column with 97.4% RH feed at 30°C.

[Color figure can be viewed in the online issue, which is available at wileyonlinelibrary.com.]

we will also adopt the "frozen front" theory[41] that the foremost edge of the water front stabilizes at CSS due to its strongly favorable isotherm shape. The cyclic water adsorption/desorption concentration curves are illustrated in Figure 10.

Based on the shock wave trajectory (Figure 10), the term on left-hand side of Eq. 3 can be simplified as

$$\int_0^{Z_W} (N_{w.i}-N_{w.f})\frac{\pi D_{in}^2\rho_b L}{4}dZ=\Delta N_w\frac{\pi D_{in}^2\rho_b L}{4}Z_w \tag{6}$$

$$\Delta N_w=N_w(P_H,T_H)-N_w(P_L,T_L) \tag{7}$$

where ΔN_w is the working capacity of water on the adsorbent in the given partial pressure envelope of $P_H \rightarrow P_L$ and the temperature range. For isothermal processes, this value can be directly calculated from the isotherm equations, whereas under nonisothermal conditions, the determination is not straightforward, as the loading is coupled with the temperature change. We consider an adiabatic process in this study, given the relatively large diameter (5 cm) of the column and good thermal insulation around the column. Therefore, the adiabatic working capacity of water ΔN_w can be derived explicitly from the isobaric diagram (Supporting Information Figure S4) or by integration of the total differential of the isotherm equation as a function of T and P in Eq. 5 as follows

$$\int_{N_L}^{N_H}\Delta H(P,T)dN=C_s(1+N(P_L,T_L))T_H - C_s(1+N(P_H,T_H)M)T_L \tag{8}$$

where the left-hand side is the integral heat from loading N_L at low pressure and low temperature to loading N_H at high pressure and temperature. M denotes the molecular weight of adsorbate and the heat capacity of adsorbate is assumed same as that of the adsorbent C_s.

For systems with constant isosteric heat, for example, single-site Langmuir or linear isotherms, the above equation becomes

$$\frac{N(P_H,T_H)-N(P_L,T_L)}{(1+N(P_L,T_L)M)T_H-N(P_H,T_H)MT_L}=\frac{C_s}{\Delta H} \tag{9}$$

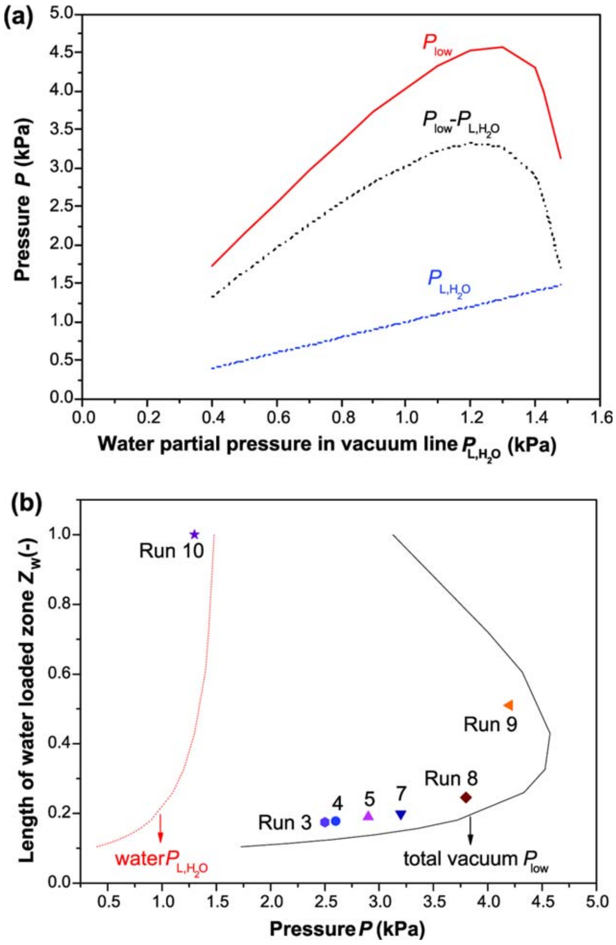

Figure 12. (a) The dependence of the lowest total vacuum pressure P_{low} on the lowest partial pressure of water vapor in the vacuum line P_{L,H_2O}; and (b) the dependence of the length of water loaded zone Z_W on the lowest vacuum pressure of the system P_{low} in 13X single-layer column with 97.4% RH feed at 30°C.

Lines are predicated results by our simple model and solid symbols are experimental data points as a function of P_{low} of individual runs. All the data are calculated/measured at 30°C except for Run 10. [Color figure can be viewed in the online issue, which is available at wileyonlinelibrary.com.]

There are four variables in Eq. 8, namely P_H, P_L, T_H, and T_L, and they vary along the bed. At the inlet of the bed, P_H and P_L are normally known for a given VSA. At the end of adsorption step, T_H is higher than the feed temperature T_F, whereas at the end of desorption step T_L is lower than T_F, and they swing across T_F with approximately equal amplitude (e.g., Supporting Information Figure S2). It is important to note that CO_2 physisorption on water loaded 13X zone is negligible, so the temperature swing in water loaded 13X zone can be attributed to H_2O adsorption/desorption only. The following assumption is made

$$\frac{T_H+T_L}{2}=T_F \tag{10}$$

The physical meaning of Eqs. 8 and 10 is that at given pressure envelop and feed temperature, the adiabatic

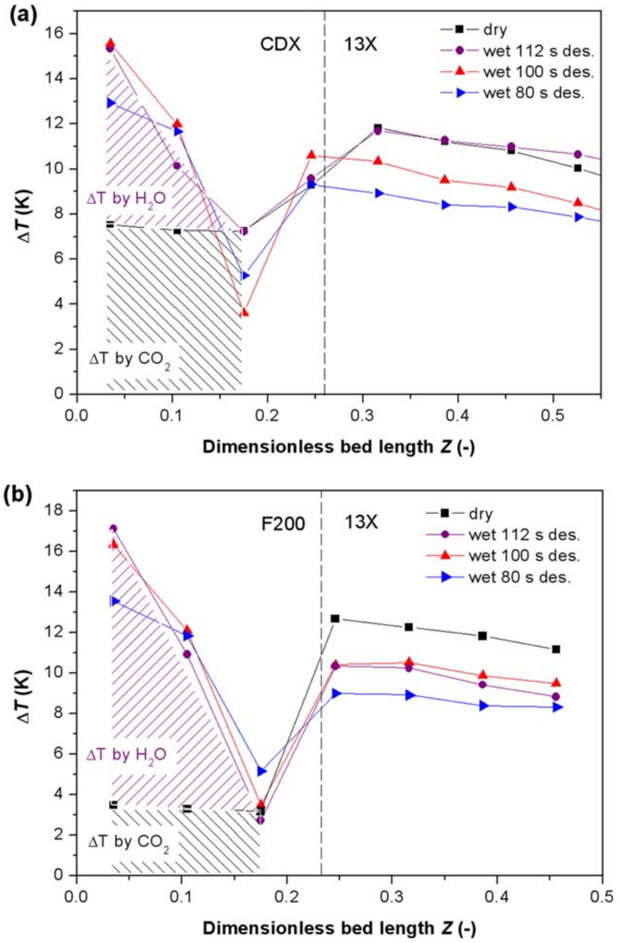

Figure 13. Temperature changes in the double-layered columns measured by individual thermocouples in a single cycle at CSS for dry CO_2 feed, and for wet feed with different desorption time: 112, 100, and 80 s.

(a) CDX/13X layering of Run 11–14; (b) F200/13X layering of Run 15–18. [Color figure can be viewed in the online issue, which is available at wileyonlinelibrary.com.]

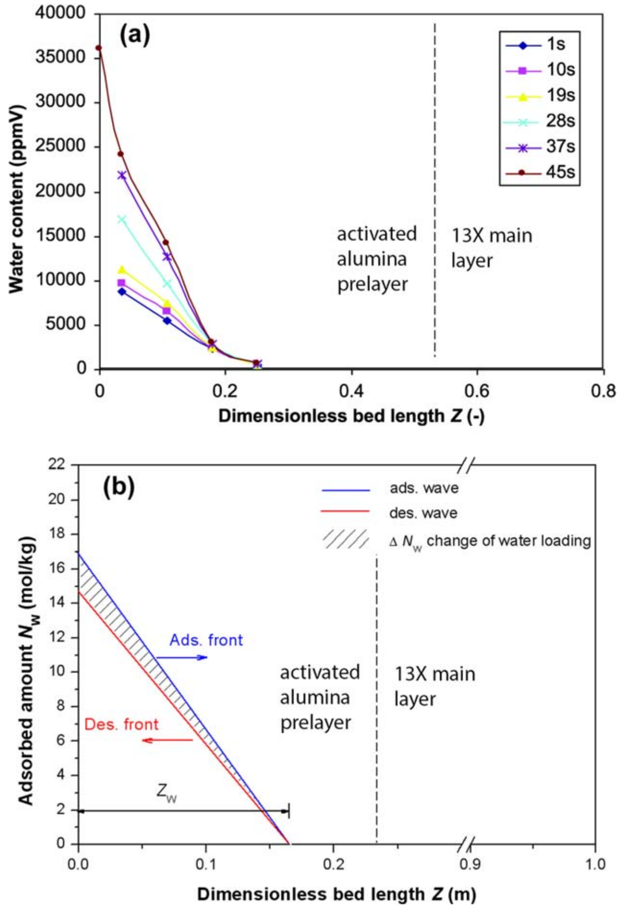

Figure 14. (a) Propagation of water concentration wave in gas phase during the adsorption step at CSS in Run 19.

(b) An illustration of the solid phase water wave front model for a typical activated alumina CDX + 13X column at CSS by using operation conditions of Run 12. [Color figure can be viewed in the online issue, which is available at wileyonlinelibrary.com.]

adsorption working capacity of the specific adsorbent is fixed. Combining Eqs. 8 and 10, we can determine the adiabatic working capacity of water ΔN_w by Eq. 7. By substituting ΔN_w into Eq. 6 and then Eq. 3, eventually, the length of water loaded zone is obtained.

Using the experimental conditions of Run 5, for example, $P_H = 3.48$ kPa, $P_L = 0.63$ kPa, and $T_F = 303.15$ K, the length of the water layer was determined as 0.125. It must be clarified that P_L represents the lowest partial pressure of water in vacuum line rather than the overall lowest vacuum pressure P_{low} in Table 1. By manipulating P_L, we can generate a range of data as plotted in Figure 11. The horizontal axis was cast into $1/P_L$ rather than P_L for comparison with Figure 3a because the volumetric flow rate is inversely proportional to P_L. The predicted results by our model (Figure 11) show a similar trend of water loaded length to experimental measurements (Figure 3a). The water front stays steady at the bottom of the column at appropriately deep vacuum. However, further deepening the vacuum will not effectively reduce the water loaded length but requires more pump work, as later suggested by comparing the energy consumption of Run S1 and S2. Herein, a critical vacuum level of water vapor exists, approximately within the range of $0.8 < P_L < 1$ kPa—analogous to the forementioned critical P/F, above which the water front tends to break through the column. The predicted water loaded length is slightly shorter than the experimental one (Run 5), probably because local equilibrium was used in the model without considering the impact of kinetics and also the real water concentration wave may have some degree of dispersion. Incorporation of a shrinking core model may better account for the kinetic effects.[51]

In a field VSA unit, determination of the lowest total pressure P_{low} in the vacuum line is critial in selection of the vacuum pump and estimation of the energy consumption of the process which is often reflected in terms of compression ratio P_{high}/P_{low}. Therefore, it is essential to find the relationship between the length of water loaded zone Z_w and the lowest pressure P_{low} of the system, when the pressure envelop of water vapor is given. As the dependence of water loaded zone Z_w on the lowest partial pressure of water P_{L,H_2O} is known from the above analysis (where P_{L,H_2O} was cited as P_L), we can easily find the relationship between P_{L,H_2O} and P_{low}, by taking mass conservation and some

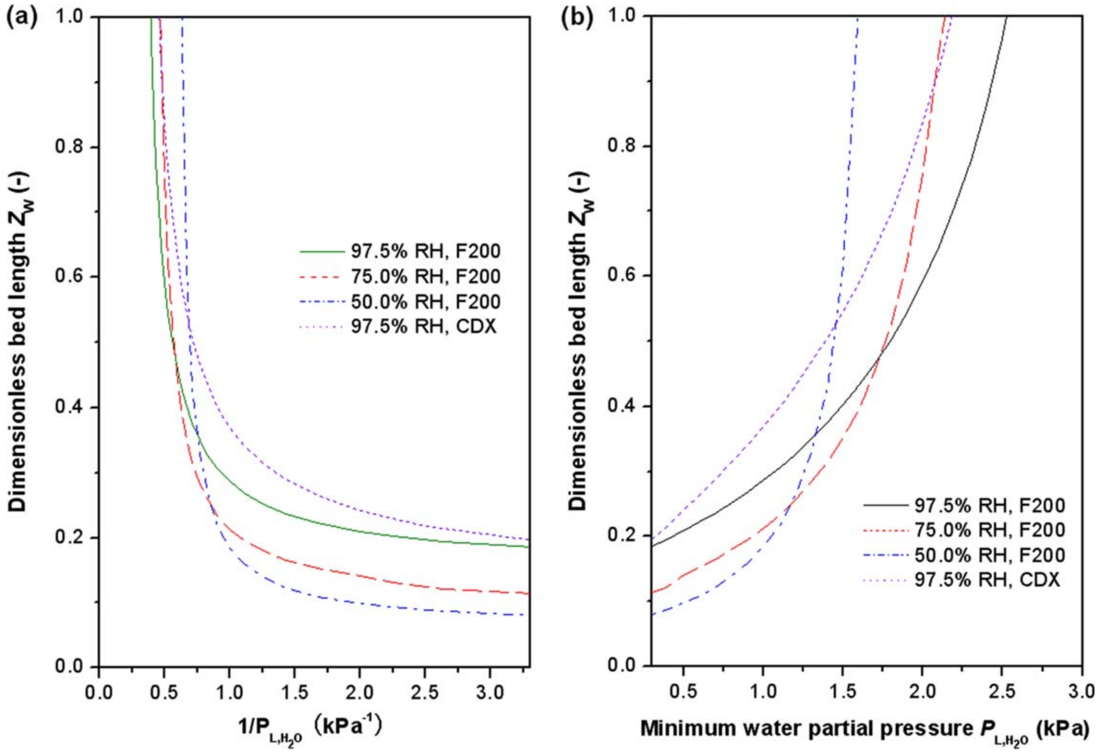

Figure 15. Dependence of water loaded zone, (a) on the reciprocal of water partial pressure, and (b) on water partial pressure, in the prelayer of activated alumina F200 and CDX, respectively.

[Color figure can be viewed in the online issue, which is available at wileyonlinelibrary.com.]

appropriate assumptions (see Supporting Information). The total vacuum pressure can be estimated as follows

$$P_{\mathrm{low}}=P_{\mathrm{L,H_2O}}\frac{N_{\mathrm{F,H_2O}}+N_{\mathrm{F,CO_2}}R_{\mathrm{CO_2,dry}}\left(1-Z_{\mathrm{w}}+\frac{1-\varphi_{\mathrm{CO_2,dry}}}{\varphi_{\mathrm{CO_2,dry}}}\right)}{N_{\mathrm{R,H_2O}}} \qquad (11)$$

where $R_{\mathrm{CO_2,dry}}$ denotes the CO_2 recovery obtained from the corresponding runs with dry feed and φ denotes the purity of recovered CO_2.

We applied this model to the case of a shock wave water front (Run 3–10) by using dry gas feed Run 2 as reference for Eq. 11. We obtained the comparison between the lowest partial pressure of water vapor in the vacuum line $P_{\mathrm{L,H_2O}}$ and the lowest total vacuum pressure P_{low} in terms of their influence on the length of water loaded zone Z_{W}. In Figure 12a, P_{low} first increases with $P_{\mathrm{L,H_2O}}$ when $P_{\mathrm{L,H_2O}} < 1.3$ kPa, and then P_{low} drops suddenly with the increase of $P_{\mathrm{L,H_2O}}$ when $P_{\mathrm{L,H_2O}} > 1.3$ kPa. The difference between P_{low} and $P_{\mathrm{L,H_2O}}$, that is, $P_{\mathrm{low}}-P_{\mathrm{L,H_2O}}$, which is the contribution of desorbed CO_2 and other inert components into the vacuum line, drops even more drastically at $P_{\mathrm{L,H_2O}} > 1.3$ kPa. The underlying physical meaning is that with increase of partial pressure of water in the vacuum line, for example, due to shortened desorption time or loss of pump capacity, the length of remaining dry zeolite layer $(1-Z_{\mathrm{W}})$ used for CO_2 capture is being dramatically shortened (Figure 12b, dashed curve) leading to less recovery of CO_2. As the loss of CO_2 is much more than the increase of water vapor under evacuation when $P_{\mathrm{L,H_2O}} > 1.3$ kPa, the total vacuum pressue P_{low} decreases while water vapor tends to break through the column, as illustrated by the solid curve in Figure 12b. The inflection point of this curve corresponds to the transformation of the process from a CO_2/H_2O VSA to a water VSA predominantly. This unusual interdependent relationship between Z_{w} and P_{low} is supported by our experimental observation (data points in Figure 12b).

Case II: Linear Dispersive Wave Front. From Figure 13, we can see that in the case of dry CO_2 feed, there were two ΔT plateaus with the one in the 13X layer higher than the one in the prelayer. That indicates the recovered amount of CO_2 was uniform in each layer within the displayed scale but differentiates across the layer boundary. After the introduction of water, the plateau in the 13X layer was not significantly altered.

It is known that the loading of CO_2 on activated alumina (F200) in the binary system is low but almost unchanged due to the enhancement effect by cooperative adsorption of H_2O, in which CO_2 was believed to have a secondary adsorption on adsorbed water layers by forming complexes with water molecules.[52] Therefore, the temperature change in the alumina prelayer as shown in Figure 13 (wet 112 s desorption) can be attributed to the summation of ΔT by CO_2 (square shaded area) and ΔT by H_2O (triangle shaded area). It can be also observed from Figure 13 that ΔT by CO_2 is the same for both dry and wet runs (112 s desorption). Subtracting the contribution of ΔT by CO_2 (this value varies with different operation conditions accordingly), we can find the reversible adsorption/desorption amount of H_2O on activated alumina prelayer decrease quasilinearly along the axial direction.

Apart from the linear ΔT profile, there are direct evidences from experiments (Figure 5) and simulations (Figures 9a and 10) in which the gas-phase water concentration front can be approximated by a wedge-shaped linear wave. In our latest VSA experiments with F200/CDX/13X triple-layered bed configuration (Run 19), we found that during the feed step

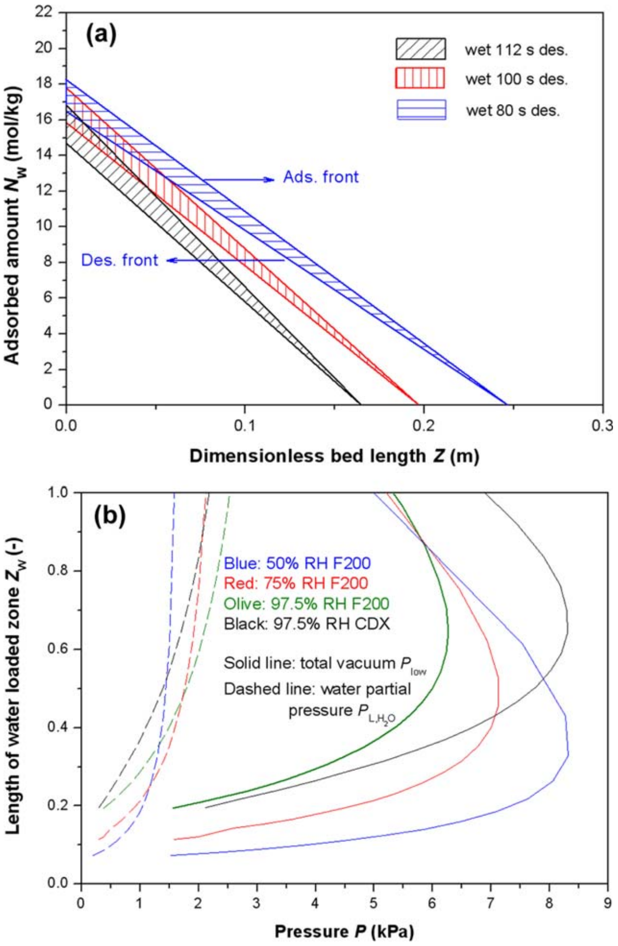

Figure 16. (a) Predicted adsorption/desorption wave front of water concentration in solid phase in Run 12 ($P_{low} = 2.89$ kPa), 13 ($P_{low} = 3.73$ kPa), and 14 ($P_{low} = 4.47$ kPa).

The results are comparable to the experimental data in Figure 11. The three shaded areas are of the same size. (b) The dependence of the length of water loaded zone Z_W on the lowest vacuum pressure of the system P_{low} (solid line) in comparison with that on the lowest water partial pressure P_{L,H_2O} (dashed line), in activated alumina/13X double layer column with a range of RH feed at 30°C. The prelayer adsorbent was alumina F200 and alumina CDX, respectively. [Color figure can be viewed in the online issue, which is available at wileyonlinelibrary.com.]

the wedge-shaped wave propagated in a manner that only the slope of the wave increased with time but the foremost edge remained frozen (Figure 14a). We believe the wedge-shaped water concentration wave is a result of the nature of the quasilinear water isotherm (Supporting Information Figure S3b) and the effect of cyclic forwards/backwards gas flow in the column. It implies that the axial distribution of the amount of water removed per cycle by activated alumina prelayer can be approximated by a "triangle" or "wedge" configuration as illustrated by the shaded area in Figure 14b, where the amount of water removed at each node ΔN_w decreases linearly along the column.

At CSS, the amount of water removed by the prelayer equals the amount of water fed to the column, the general analytical approach described by Eq. 3 is valid. The left side of Eq. 3 can be expressed as

$$\int_0^{Z_W} (N_{w,i} - N_{w,f}) \frac{\pi D_{in}^2 \rho_b L}{4} dZ = \Delta N_w \frac{\pi D_{in}^2 \rho_b L}{8} Z_W \qquad (12)$$

which is the modified version of Eq. 6 for characterising axial working capacity with "triangle" configurations. By assuming adiabatic operation and validation of the simple energy balance Eq. 5, we can use the same approach in Case I to determine the adiabatic working capacity of water ΔN_w (Eqs. 8 and 10). The isotherm equations of water on corresponding materials are available from our previous study.[52,53] In addition, the impact of coadsorbed CO_2 on water adsorption is negligible. Substituting ΔN_w into Eq. 12 will give the length of water loaded zone. We use experimental conditions of Run 12 ($P_{L,H_2O} = 0.4346$ kPa) and Run 16 ($P_{L,H_2O} = 0.444$ kPa) as input information for the above model and the calculated results are demonstrated in Figure 15. The general trend of the water loaded length in activated alumina prelayers against the reciprocal of the P_{L,H_2O} of water vapor is not as steep as that in the single-layered 13X column (Figure 11), which means the processes using activated alumina prelayers are more robust at varing humidities. From Figure 15, it can be seen that under the same operating conditions, compared with F200 prelayer, a thicker prelayer of CDX is required to prevent water penetration into the main layer; above the critical $1/P_{L,H_2O}$, lower feed relative humidity will generate a shorter water zone. However, the critical $1/P_{L,H_2O}$ decrease with rising feed water content, indicating even smaller partial pressure of water vapor P_{L,H_2O} is required to cope with lower feed relative humidity. This feature is of particular concern in the case of a liquid ring vacuum pump whose vacuum level is limited by the saturation pressure of the working fluid, imposing a risk of process failure in hot weather. However, the deficiency of the vacuum pump can be possibly compensated by the large amount of internal purge gas (mainly CO_2) which can substantially reduce the partial pressure of H_2O (Figure 7) in the case of high concentration CO_2 in feed, for example, 35% CO_2 in Run S5, Figure 9a. Conversely, shorter evacuation time will lead to higher P_{L,H_2O} and smaller ΔN_w, and thus the water front will propagate further into the bed as expected (Figure 16a). By applying Eq. 11 to the multilayered VSA runs, the interdependent relationship between the deepest vacuum pressure P_{low} and the penetration dependence of water vapor in the column Z_w can be determined, as shown in Figure 16b. At low Z_w range, Z_w increases with P_{low}, whereas in the high Z_w range P_{low} becomes even smaller. This special feature is very similar to what we have discussed earlier in the single-layered column (Figure 12) and the underlying mechanism is same. By comparing the curve of total vacuum pressure P_{low} in Figure 16b with that in Figure 12, we can see that the column using an activated alumina prelayer can tolerate a larger P_{low} pressure than the one without prelayer. This means the adoption of a water removal prelayer can potentially save a considerable amount of vacuum pump in a CO_2/H_2O VSA process. Therefore, the partial pressure of water vapor in the vacuum line P_{L,H_2O} is a function of pump capacity, internal purge, and evacuation time. The dimensionless water loaded length is independent of the feed step time or the absolute bed length but depends on the feed composition, temperature, and evacuation pressure which are practically covered by the purge-to-feed ratio, as well as the physical properties of the adsorbents, such as isotherm shape, heat capacity, bulk density and so forth. Therefore, the optimal ratio of "prelayer-to-main layer"—λ is defined as the ratio between the length of the two layers when CO_2 is recovered at an appropriate purity and recovery by the main layer (as determined from dry CO_2 VSA, e.g., Run 2) and meanwhile H_2O is just exactly 100% recovered by the prelayer without any unused bed length and this ratio can be formulated as follows

$$\lambda = \frac{Z_w}{1-Z_w} \tag{13}$$

In real operations, λ should be determined by taking into account the most conservative circumstances with some safety margin.

Conclusions

In this study, we have demonstrated that CO_2 can be effectively captured from highly humid postcombustion flue gases by VSA with multilayered columns. Activated alumina F200 and CDX are good candidates for the prelayer adsorbents because of their quasilinear water isotherms which endow them with higher working capacities under VSA conditions, while zeolite 13X still remains one of the best commercial adsorbents for carbon capture in the main layer. Our experiments and computer simulations suggests the key factors controlling the performance of the CO_2/H_2O VSA process are volumetric purge-to-feed ratio and layering strategy of the adsorbents.

The volumetric P/F ratio has been examined for VSA processes particularly with little external purge. Water can be successfully removed along with the CO_2 stream by maintaining an appropriate volumetric P/F ratio, where the water front stabilizes in the bed. However, when the P/F ratio is lower than the critical value, water tends to penetrate the column and there is a high risk of process failure. The volumetric P/F ratio is a lumped parameter capturing the effects of feed and evacuation conditions. The feed CO_2 concentration, evacuation time, and vacuum level contribute positively to the P/F ratio, whereas feed H_2O concentration impacts negatively. Of particular importance, dry CO_2 desorbed from the main layer plays a role of internal purge, which is essential to lowering the water partial pressure during the evacuation step and the relatively hotter CO_2 gas also brings the heat from the main layer of the column to facilitate the desorption of water in the prelayer.

The length of water loaded zone is a major criteria to evaluate the effectiveness of water removal by the prelayers. We developed an axial adiabatic working capacity model to estimate the penetration depth of water in the column, based on a simple mass and energy blance using an analytical approach. The model has been successfully applied to two types of water wave fronts: (1) shock wave for adsorbents with sharp Type I isotherms; (2) linear dispersive wave for materials with linear or quasilinear isotherms. It was predicted by the model that the length of the water loaded zone increased exponentially with the elevation of the lowest partial pressure of water (P_L) in the vacuum line, suggesting the existance of a critical P_L above which the water front becomes unbounded. As P_L is normally a preset operation constraint, the length of water loaded zone can be resolved by the model and then, the required minimum layering ratio (prelayer:main layer) can be determined. The layering ratio is of particular importance in designing a layered column at given operation conditions.

For low to medium humidity feed, double-layered columns are more effective than single-layered ones in terms of CO_2 capture. However, at high humidity (>8.5% v/v), reasonably good performance can be achieved with our strategy of novel triple-layered column by maximizing the efficiency of the adsorbents—making the first prelayer dedicated to water removal, the second prelayer effective for water and CO_2, and the main layer targeted for CO_2. Extrapolation of this process to multicolumns and full process steps. To further reduce the capture cost, system integration is also possible for industrial scale capture process by means of: (1) heat integration, such as recovering the high exergy contained in the massive CO_2-removed dry flue gases from the VSA units, for example, brown coal drying and adsorbents regeneration; (2) materials recycle, such as making use of the large amount of liquid water collected by the vacuum pump. The ultimate strategy to solve the detrimental effect of H_2O is to use water tolerant/hydrophobic CO_2 adsorbents. However, the development of such materials is extremely challenging.

Acknowledgments

The author G. Li is grateful for the Early Career Development Fellowship provided by Monash University. Funding for this CO2CRC project is provided by the Australian Government through its CRC program.

Notation

c = gas-phase concentration, mol/m3
$\bar{c}$ = instantaneous gas-phase concentration, mol/m3
C_s = sorbent heat capacity, kJ/kg K
CDX = a type of activated alumina
CSS = cyclic steady state
D_{in} = inner diameter of the adsorption column, mm
F200 = a type of activated alumina, same as F-200
ΔH = heat of adsorption, kJ/kg
K = LDF coefficient, 1/s.
K = Henry law constant
L = length of the adsorbents in column, m
LDF = linear driving force
MINSA = Melbourne integrated numerical simulator for adsorption
N = adsorbed amount, mol/kg
P = pressure, kPa or bar
P_L = the lowest partial pressure of a component (H_2O) in evacuation step, kPa
P_{L,H_2O} = the lowest partial pressure of water vapor in evacuation step, kPa
P_{low} = the lowest total pressure in evacuation step, kPa
ppm = part per million
PSA = pressure swing adsorption
P/F = purge to feed ratio
R = gas constant, J/mol/K
RH = relative humidity
T = temperature, °C
v = volumetric flow rate, m3/s
VSA = vacuum swing adsorption
y = mole fraction in gas phase
Z = dimensionless bed distance

Greek letters

ε = voidage
λ = layering ratio
M = molecular mass, g/mol
ρ = density, kg/m^3
φ = purity

Subscripts and superscrits

b = bed
f = final state

F = feed
H = high
i = initial state
in = inlet
L = low
out = outlet
P = purge
R = recovered
s = solid phase
t = total
w = water
$*$ = equilibrium state

Literature Cited

1. Kikkinides ES, Yang RT, Cho SH. Concentration and recovery of CO2 from flue-gas by pressure swing adsorption. *Ind Eng Chem Res.* 1993;32:2714–2720.
2. Chue KT, Kim JN, Yoo YJ, Cho SH,Yang RT. Comparison of activated carbon and zeolite 13X for CO_2 recovery from glue-gas by pressure swing adsorption. *Ind Eng Chem Res.* 1995;34:591–598.
3. Zhang J, Webley PA, Xiao P. Effect of process parameters on power requirements of vacuum swing adsorption technology for CO_2 capture from flue gas. *Energy Convers Manage.* 2008;49:346–356.
4. Zhang J, Webley PA, Xiao P. Experimental pilot-scale study of carbon dioxide recovery from flue gas streams by vacuum swing adsorption. *AIChE* 2005 Annual Meeting. Cincinnati, 2005.
5. Liu Z, Grande CA, Li P, Yu J, Rodrigues AE. Multi-bed vacuum pressure swing adsorption for carbon dioxide capture from flue gas. *Sep Purif Technol.* 2011;81:307–317.
6. Li G, Xiao P, Webley P, Zhang J, Singh R, Marshall M. Capture of CO_2 from high humidity flue gas by vacuum swing adsorption with zeolite 13X. *Adsorption.* 2008;14:415–422.
7. Zhang J, Xiao P, Li G, Webley PA. Effect of flue gas impurities on CO_2 capture performance from flue gas at coal-fired power stations by vacuum swing adsorption. *Energy Procedia.* 2009;1:1115–1122.
8. Brandani F, Ruthven DM. The effect of water on the adsorption of CO2 and C3H8 on type X zeolites. *Ind Eng Chem Res.* 2004;43:8339–8344.
9. Liang ZJ, Marshall M, Chaffee AL. CO_2 adsorption-based separation by metal rrganic framework (Cu-BTC) versus zeolite (13X). *Energy Fuels.* 2009;23:2785–2789.
10. Hicks JC, Drese JH, Fauth DJ, Gray ML, Qi GG, Jones CW. Designing adsorbents for CO_2 capture from flue gas-hyperbranched aminosilicas capable of capturing CO_2 reversibly. *J Am Chem Soc.* 2008;130:2902–2903.
11. Subagyono DJN, Liang Z, Knowles GP, Chaffee AL. Amine modified mesocellular siliceous foam (MCF) as a sorbent for CO_2. *Chem Eng Res Des.* 2011;89:1647–1657.
12. Sayari A, Heydari-Gorji A, Yang Y. CO_2-induced degradation of amine-containing adsorbents: reaction products and pathways. *J Am Chem Soc.* 2012;134:13834–13842.
13. Wang Y, LeVan MD. Adsorption equilibrium of binary mixtures of carbon dioxide and water vapor on zeolites 5A and 13X. *J Chem Eng Data.* 2010;55:3189–3195.
14. Kumar R, Huggahalli M, Deng S, Andrecovich M. Trace impurity removal from air. *Adsorption.* 2003;9:243–250.
15. Rege SU, Yang RT, Qian KY, Buzanowski MA. Air-prepurification by pressure swing adsorption using single/layered beds. *Chem Eng Sci.* 2001;56:2745–2759.
16. Ribeiro AM, Grande CA, Lopes FVS, Loureiro JM, Rodrigues AE. Four beds pressure swing adsorption for hydrogen purification: case of humid feed and activated carbon beds. *AIChE J.* 2009;55:2292–2302.
17. Ahn H, Lee CH. Adsorption dynamics of water in layered bed for air-drying TSA process. *AIChE J.* 2003;49:1601–1609.
18. Cavenati S, Grande CA, Rodrigues AE. Layered pressure swing adsorption for methane recovery from $CH_4/CO_2/N_2$ streams. *Adsorption.* 2005;11:549–554.
19. Cavenati S, Grande CA, Rodrigues AE. Separation of $CH_4/CO_2/N_2$ mixtures by layered pressure swing adsorption for upgrade of natural gas. *Chem Eng Sci.* 2006;61:3893–3906.
20. Chlendi M, Tondeur D. Dynamic behavior of layered columns in pressure swing adsorption. *Gas Sep Purif.* 1995;9:231–242.
21. Jain R, Deng S. Removal of carbon dioxide from air. EP0904825. The BOC Group Inc., US, 1999.
22. Klein G, Vermeulen T. Cyclic performance of layered beds for binary ion exchange. *AIChE Symp Ser.* 1975;71:69–76.
23. Lee CH, Yang JY, Ahn HW. Effects of carbon-to-zeolite ratio on layered bed H_2 PSA for coke oven gas. *AIChE J.* 1999;45:535–545.
24. Malek AH, Farooq S. Hydrogen purification from refinery fuel gas by pressure swing adsorption. *AIChE J.* 1998;44:1985–1992.
25. Park JH, Kim JN, Cho SH. Performance analysis of four-bed H2 PSA process using layered beds. *AIChE J.* 2000;46:790–802.
26. Park JH, Kim JN, Cho SH, Kim JD,Yang RT. Adsorber dynamics and optimal design of layered beds for multicomponent gas adsorption. *Chem Eng Sci.* 1998;53:3951–3963.
27. Wilson SJ, Webley PA. Cyclic steady-state axial temperature profiles in multilayer, bulk gas PSA – the case of oxygen VSA. *Ind Eng Chem Res.* 2002;41:2753–2765.
28. Yang JY, Lee CH. Adsorption dynamics of a layered bed PSA for H2 recovery from coke oven gas. *AIChE J.* 1998;44:1325–1334.
29. Tseng JK, Jain R. *Air purification process.* US05906675. The BOC Group Inc., US, 1999.
30. Ahn H, Lee CH. Effects of capillary condensation on adsorption and thermal desorption dynamics of water in zeolite 13X and layered beds. *Chem Eng Sci.* 2004;59:2727–2743.
31. Nikolić D, Kikkinides ES, Georgiadis MC. Optimization of multibed pressure swing adsorption processes. *Ind Eng Chem Res.* 2009;48:5388–5398.
32. Pigorini G, LeVan MD. Equilibrium theory for pressure swing adsorption. 2. Purification and enrichment in layered beds. *Ind Eng Chem Res.* 1997;36:2296–2305.
33. Webley PA, He JM. Fast solution-adaptive finite volume method for PSA/VSA cycle simulation; 1 single step simulation. *Comput Chem Eng.* 2000;23:1701–1712.
34. Chan YNI, Hill FB, Wong YW. Equilibrium theory of a pressure swing adsorption process. *Chem Eng Sci.* 1981;36:243–251.
35. Da Silva FA, Rodrigues AE. Propylene/propane separation by vacuum swing adsorption using 13X zeolite. *AIChE J.* 2001;47:341–357.
36. Doong SJ, Yang RT. Bulk separation of multicomponent gas mixtures by pressure swing adsorption: pore/surface diffusion and equilibrium models. *AIChE J.* 1986;32:397–410.
37. Yang RT, Doong SJ. Gas separation by pressure swing adsorption: a pore-diffusion model for bulk separation. *AIChE J.* 1985;31:1829–1842.
38. Zhang J, Webley PA. Cycle development and design for CO2 capture from flue gas by vacuum swing adsorption. *Environ Sci Technol.* 2008;42:563–569.
39. Shendalm Lh, Mitchell JE. Study of heatless adsorption in model system CO2 in He, I. *Chem Eng Sci.* 1972;27:1449–1458.
40. LeVan MD. Pressure swing adsorption: equilibrium theory for purification and enrichment. *Ind Eng Chem Res.* 1995;34:2655–2660.
41. Wilson SJ, Beh CCK, Webley PA, Todd RS. The effects of a readily adsorbed trace component (water) in a bulk separation PSA process: the case of oxygen VSA. *Ind Eng Chem Res.* 2001;40:2702–2713.
42. Glueckauf E, Coates JI. Theory of chromatography. Part IV. The influence of incomplete equilibrium on the front boundary of chromatograms and on the effectiveness of separation. *J Chem Soc.* 1947:1315–1321.
43. Glueckauf E. Theory of chromatography. Part 10.Formulae for diffusion into spheres and their application to chromatography. *Trans Faraday Soc.* 1955;51:1540–1551.
44. Matz MJ, Knaebel KS. Temperature front sensing for feed step control in pressure swing adsorption. *Ind Eng Chem Res.* 1987;26:1638–1645.
45. Getty RJ, Armstrong WP. Drying air with activated alumina under adiabatic conditions. *Ind Eng Chem Process Des Dev.* 1964;3:60–65.
46. Serbezov A. Adsorption equilibrium of water vapor on F-200 activated alumina. *J Chem Eng Data.* 2003;48:421–425.
47. Zholobov VV, Zholobova LG. Simple wave equations of one-dimensional motion of a gas-dust mixture. *J Appl Mech Tech Phys.* 1978;19:324–330.
48. Karsten-Bär N, Balcom BJ, Ruthven DM. Direct measurement of transient concentration profiles in molecular sieve particles and columns by MRI. In: Do DD, editor. Adsorption Science and Technology. World Scientific Publishing Co. Pte. Ltd., Singapore, 2000:6–13.

49. Prado PJ, Balcom BJ, Jama M. Single-point magnetic resonance imaging study of water adsorption in pellets of zeolite 4A. *J Magn Reson*. 1999;137:59–66.
50. Zhang J, Singh R, Webley PA. Alkali and alkaline-earth cation exchanged chabazite zeolites for adsorption based CO2 capture. *Micropor Mesopor Mater*. 2008;111:478–487.
51. Yagi S, Kunii D. Studies on combustion of carbon particles in flames and fluidized beds. *Symp (Int) Combus*. 1955;5:231–244.
52. Li G, Xiao P, Webley P. Binary adsorption equilibrium of carbon dioxide and water vapor on activated alumina. *Langmuir*. 2009;25:10666–10675.
53. Li G, Xiao P, Webley PA, Zhang J, Singh R. Competition of CO2/H2O in adsorption based CO2 capture. *Energy Procedia*. 2009;1:1123–1130.

Manuscript received May 6, 2013, and revision received Oct. 10, 2013.